IEEE Access
Multidisciplinary | Rapid Review | Open Access Journal

Received December 31, 2020, accepted January 6, 2021, date of publication January 8, 2021, date of current version February 1, 2021.

Digital Object Identifier 10.1109/ACCESS.2021.3050418

An Effective Method for Detection of Demagnetization Fault in Axial Flux Coreless PMSG With Texture-Based Analysis

MEHMET RECEP MİNAZ[1] AND EYYÜP AKCAN[1,2]
[1]Department of Electrical and Electronics Engineering, Siirt University, 56100 Siirt, Turkey
[2]Batman Vocational and Technical Anatolian High School, 72100 Batman, Turkey

Corresponding author: Mehmet Recep Minaz (mehmetrecepminaz@siirt.edu.tr)

This work was supported by the Special Electrical Laboratory, Siirt University.

ABSTRACT Due to its high power densities and compact dimensions, the axial flux coreless permanent magnet synchronous generator (PMSG) is used in a wide range of areas such as wind turbines and electric vehicles. It is extremely important to detect magnetization faults that occur in these generators. The occurrence of such faults in these machines with a wide range of areas of use affects their operation negatively. In this study, an effective method has been proposed to detect the demagnetization fault occurring in axial flux coreless PMSGs. The relevant method proposes an effective texture analysis-based feature extraction method, which is an original method in contrast to conventional methods used in the literature. It has been revealed that it is a method that can be used instead of conventional methods such as time-frequency analysis, frequency spectrum analysis, and motor current signature analysis (MCSA) methods. Using the finite element method, current and voltage signals were taken from the healthy and axial flux coreless PMSG with 3% and 6% demagnetization fault. Besides, these signals were retaken at different speeds and loads. After the signals were converted into images, using the features obtained from the images with LBP, fault diagnosis processes were carried out with Knn. It was tested both at different fault rates and under different load and speed conditions to test whether the proposed method worked properly. The success rate of this method was observed as 97.16% and 100%. With the proposed method, it has been revealed that the demagnetization fault can be detected in axial flux coreless PMSGs.

INDEX TERMS Image texture analysis, demagnetization, fault detection, permanent magnet machines.

I. INTRODUCTION

The axial flux coreless PMSG has many advantages. Thus, it is commonly used. As the generator has no core, there are no core losses in the stator part. The axial flux coreless PMSG has been the center of attention with many advantages such as being more efficient than other generators, high torque, high power density, and ease of control [1]–[3]. Also, it is preferred by manufacturers in electric vehicles, industrial robots, and aviation [4], [5]. It is extremely important to diagnose machines with a huge number of application areas. Faults that may occur in these machines may affect the sensitivity. Therefore, the pre-diagnosis of faults becomes important in the axial flux coreless PMSG.

The associate editor coordinating the review of this manuscript and approving it for publication was Jinquan Xu.

Faults that occur in permanent magnet machines can be classified into three categories as stator faults, bearing faults, and rotor faults. The stator fault includes a short circuit between windings, phase-to-phase short circuit, phase-to-ground short circuit, and open circuit faults. Bearing faults include inner bearing faults, outer bearing faults, and ball faults. Rotor faults include eccentric and demagnetization faults. In addition, due to the permanent magnets that are used, the fragility and magnetization effect of the magnets decrease depending on the time and operating conditions [6]–[8].

Since the rotor used in radial flux permanent magnet machines is made of a permanent magnet, it is easy and flexible with an additional improved power factor. However, this type of machine poses great risks in real operating situations due to the faults in magnets. Therefore, monitoring magnetic

faults is essential. Demagnetization faults in Permanent Magnet Machines are usually caused by load situations that require high starting torque. Armature reaction occurs during rapid transitions from a non-stationary state to a stationary state. Backward magnetic fields caused by currents passing through the stator windings and high temperatures that occur in winding fault cause demagnetization fault [9]–[11]. Also, if the temperature in the machine exceeds the curie temperature, the effect of the permanent magnet decreases. However, even below the curie temperature, overloading, faults in the inverter, and stator windings can lead to demagnetization [12]–[15]. When the machine runs, the total flux linkage decreases depending on the increase in temperature. The total flux is considered stable in permanent magnet machine designs. However, in the flux fluctuation here, the output torque may also cause instability. The demagnetization fault occurs when the permanent magnet exceeds the critical temperature, and unless the flux density reaches its actual value. This demagnetization causes the machine to have a fault and to show low performance [16], [17]. Another reason is fractures and cracks in permanent magnets. This situation consists of unsuitable production conditions and is likely to create negative effects such as noise, vibration, and magnetic pull on the machine [18]. For these reasons, it is necessary to detect the demagnetization faults that may occur in permanent magnet synchronous machines. It is important to fix these faults for a better performance of the machine.

An accurate demagnetization analysis is required for the detection of the demagnetization fault that may occur in the machine. Many researchers have examined these fault features from different perspectives. Permanent magnet total flux (flux linkage) estimates are reported for the analysis of rate hormones under different loads, speeds, and temperatures in [19]. When using these methods, the use of information about only one characteristic may not be sufficient for fault detection [20]. For fault detection, characteristic information including magnetic flux, current, voltage, acoustic sounds, temperature, vibration, and moment is needed. Many methods are recommended in the literature for demagnetization fault detection. There are successful methods suggested in the literature that are used for fault detection.

Although the literature contains a wide range of information about the detection of demagnetization faults from radial smart machines, it has a limited number of studies on faults in the axial flux coreless PMSG. In Reference [21], an analytical method was presented to fix the fault in AFPM. In Reference [22], a new structure was proposed by modeling the three-dimensional AFPM demagnetization fault with static and dynamic eccentric defects and by comparing the experimental results with the finite element method. In addition, the zero-sequence voltage component (ZSVC) spectra of the AFPM machine were investigated by using the stator current and torque three-dimensional finite element method [23].

MCSA demagnetization is a widely used method in fault detection using torque, speed, current, and voltage data. The demagnetization fault detection in the multiphase PMSM using the MCSA-based technique was made by applying a wavelet transform (WT). The results obtained provided an effective solution [24]. Stator currents were analysed with Fast Fourier Transform (FFT) and applied to the demagnetization fault detection by analysing certain harmonics. However, they cannot be applied to non-stationary signals and cannot distinguish harmonics caused by demagnetization from harmonics caused by eccentric [25], [26]. In another study that used The Hilbert-Huang Transform (HHT) method, digital signal processing (DSP) fault diagnosis and fault detection were facilitated. The HHT algorithm provides information about operating status and changes apart from fault detection [27]. Its effects on the machine depending on the demagnetization fault were discussed. In this study, given the effects of this fault on machine voltage and current, it was determined that it produces harmonics.

In the demagnetization fault detection, Zhu *et al.* first proposed a torque wave model taking into account the electromagnetic noise in a study. Then, taking the electromagnetic disturbances into account, the data were processed with wavelet transform. Vold–Kalman was introduced to monitor the torque fluctuation sequence of the PMSM to extract the torque wave characteristic that reflects the changes in magnet state with filtering order tracking. Finally, it was used to train the Dynamic Bayesian Network (DBY) for detecting and predicting demagnetization during machine runtime. With this method, the demagnetization fault was detected very well in a wide speed range [28]. Demagnetization diagnosis was attempted by using continuous wavelet transforms (CWT) and gray system theory (GST). By using CWT, the effect of electromagnetic interference was eliminated. Demagnetization rates using GST and torque fluctuation caused by demagnetization made it easier to detect the energy vibrations. With this method, the demagnetization fault detection was performed in different operating conditions and real-time [29]. In a study conducted with the texture analysis method, it was observed that high success was achieved in the detection of bearing fault. [30]–[35]. In a wind turbine application, fault detection and classification were made by using the texture analysis method. High accuracy was obtained [36].

Studies have shown that texture-based analysis can be successful in fault detection. Therefore, this method has been used for demagnetization fault detection. There are studies using current and voltage data for demagnetization fault detection. It is noteworthy that this data is easier to record and process than data such as vibration. It has also been revealed that recording this data is less costly. In this study, an effective fault detection method has been proposed by using current and voltage data. A great success was achieved in the fault detection with the effective texture-based analysis-based method. With this method, current and voltage signals were analyzed in the time domain and the feature was extracted. Thus, faster results were obtained. The features obtained in this study provided a success rate between 97.16% and 100%.

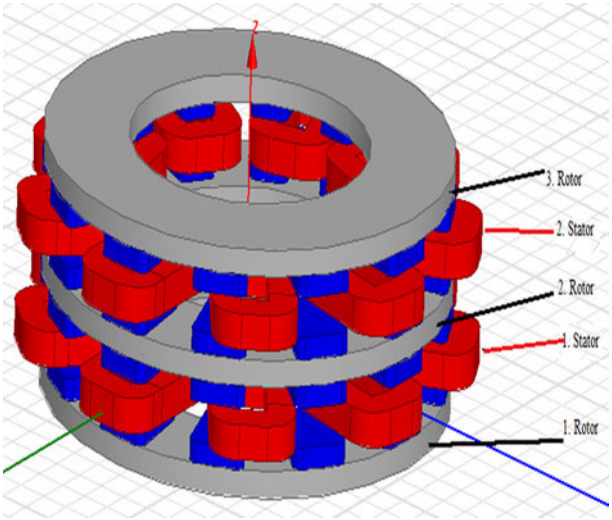

FIGURE 1. Axial flux coreless PMSG test model with three rotors and two stators [1].

TABLE 1. Parameters of the Test Generator.

Rated power, *kW*	1,8
Number of phases	3
Rated Torque, *Nm*	39,4
Number of poles	12
Winding inductance, *mH*	1.76
Phase resistance, Ω	1.72
Rated Speed, *rpm*	500

II. TEST BENCH SETUP

In order to diagnose the demagnetization fault that may occur in the machine, current and voltage fault signals were compared with healthy signals. Analyses were made using the finite element method to obtain current and voltage signals for healthy and faulty situations at different speeds and loads. One of these generators was healthy, while 3% and 6% demagnetization fault was given to one of them and the other of them, respectively. In the analysis made with the finite element method, 3D views are given in the machine used in Figure 1.

Parameters of the generator are given in Table 1 [1].

III. METHOD

A. PROPOSED METHOD

This study proposes a completely different approach from previous studies for the fault detection from the signals obtained under different speed and load conditions from axial flux coreless PMSGs. A block diagram of the proposed method is given in Fig.2.

Blok 1: It indicates raw signals obtained at different loads and speeds from axial flux coreless PMSGs with different fault severities. These are signals measured at different speeds, loads, and fault rates.

Blok 2: The pixel values of two-dimensional gray images vary between 0-255. To convert the signals to images, the signal values must be converted to values in this range. The following equation is used to indicate values on the signal X_i and to convert the signals to values between 0-255. There is no change in the appearance of the signal after the conversion. A sample conversion is given in Fig.3.

Blok 3: At this stage, the signals obtained from the magnet motors are converted to images. Depending on the length of the signals, these signals are converted to images of size NxM. A sample conversion process is shown in Figure.

Block 4: It is the step during which the LBP method is applied to the gray images obtained. Section B describes how the LBP method is applied to images.

Block 5: After the LBP method is applied to gray images, LBP features are obtained from new images. These feature vectors are used as input features for classification methods.

Block 6: It is the classification step. In this study, the Knn- (K nearest neighbor) machine learning method was used as a classifying method. The classification was performed according to the 10-fold cross-validation test. **Block 7**: It is the step of decision and fault detection.

$$NewX_i = round\left(\left[\frac{x_i - \min(x)}{Max(x) - Min(x)}\right] \times 255\right) \quad (1)$$

The sample conversion of a signal to a gray image is shown in Fig.5. As seen from the figure, a textural image is obtained. The conversion in Figure 5 belongs to the current signals obtained from the single phase of the faulty and healthy motor by 3%, which are running at 0 loads and 300 rpm.

B. LOCAL BINARY PATTERN

The local binary pattern (LBP) texture analysis operator is a gray-level independent texture measure method. The original LBP operator creates a label for each pixel of the image. This label is a binary number that is obtained by comparing the central pixel to the pixels in the 3 × 3 neighborhood. Each pixel from the image is obtained by binarizing the difference between itself and its neighbors with the step function. The LBP operator characterizes the relationship between the pixels in the image (X_p, X_c). This operator is expressed by the following equation [37].

Where X_c indicates the centre pixel, X_c is, the centre pixel's neighbors, R is, the distance of the neighbors from the centre pixel, and P is the number of neighboring operands. This structure shows that various circular neighborhoods can be used. Thus, it is possible to perform the analysis of textures of different sizes with LBP. [38]. Fig. 6 gives an example of tagging pixels with the LBP operator.

$$LBP_{P,R}(x_c) = \sum_{p=0}^{p-1} \mu\left(x_p - x_c\right)2^p,$$
$$\mu(y) = \begin{cases} 1, & y \geq 0 \\ 0, & y < 0 \end{cases} \quad (2)$$

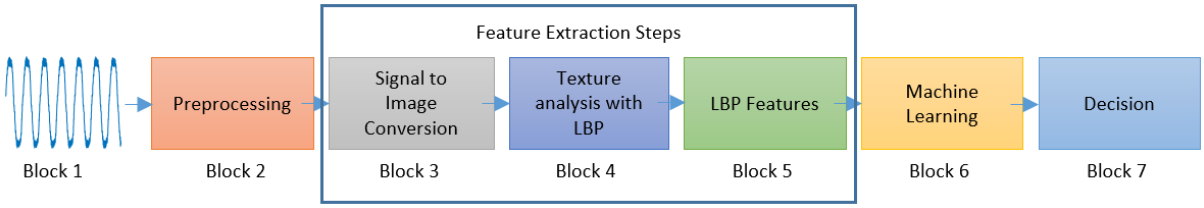

FIGURE 2. Block diagram belonging to the proposed method.

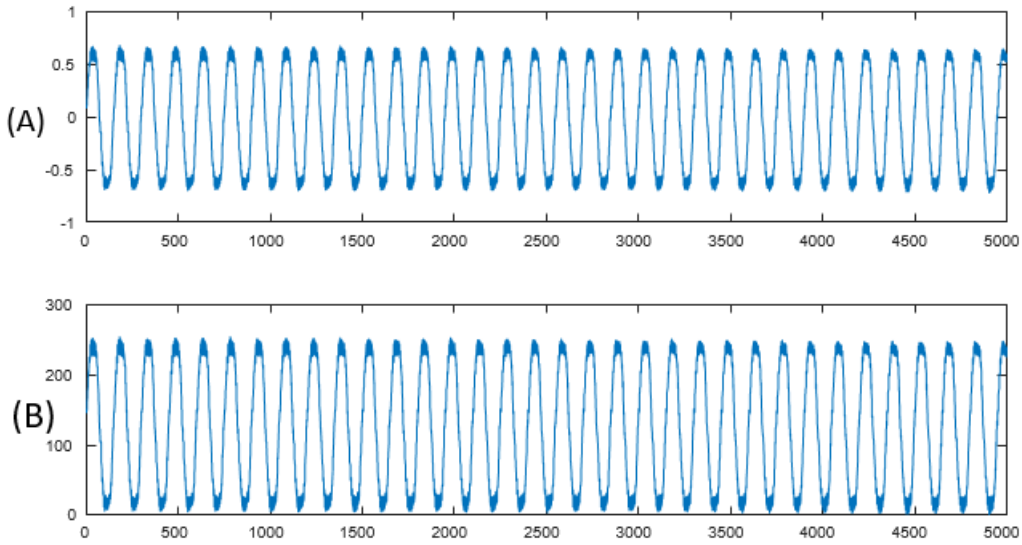

FIGURE 3. Conversion of signals to values ranging between 0-255.

Not all the LBP values created are used in the texture analysis. The uniform patterns used in the identification are those having 2 or less 0-1 or 1-0 transitions in the binary LBP code. For example, the patterns 000000 and 111111 are uniform as they contain 0 transition and the patterns 011000 and 110011 are uniform as they have 2 transitions. However, the patterns 010100 with four transitions and 010101 with five transitions are not uniform. Studies have shown that a large proportion of the surfaces of the texture investigated consist of uniform patterns [39]–[42].

As uniform patterns are used when extracting the LBP histogram, all non-uniform patterns are used as a feature while it refers to a feature for each uniform pattern in the histogram. When all patterns are examined, 256 different codes are formed for 8 neighborhoods, and 58 of them are uniform. In this case, the LBP histogram has 59 partitions.

The LBP has two important parameters. The first parameter of the LBP is P, which specifies the number of neighbors. Large values of P in the creation of the LBP image both enlarge the feature histogram and increase the transaction cost. Small values of P can cause a significant amount of information loss. The second parameter of the LBP is the scale (R) parameter. R indicates the distance of neighboring pixels from the center pixel [43], [44].

IV. RESULTS

In this study, an effective approach of axial flux coreless PMSG has been proposed to determine whether the generator is faulty or healthy from the signals obtained from the healthy and faulty generator under different speed and load conditions, and from the current and voltage signals. In this method, firstly the signals obtained from the generator are transformed into two-dimensional gray-scale images. The signals in the time domain can be converted into images in desired MxN dimensions. The dimension of the image can be adjusted according to the length of the signals. However, the dimensions of the image must be of a dimension that includes meaningful expressions. In sample transformations in this study, the signals were transformed into 100 × 100 grayscale images.

The tables in the findings section show the results of the fault detection using current and voltage signals obtained during the operation of the axial flux coreless PMSG under different speed and load conditions. The tables obtained here show separate results for each current and voltage

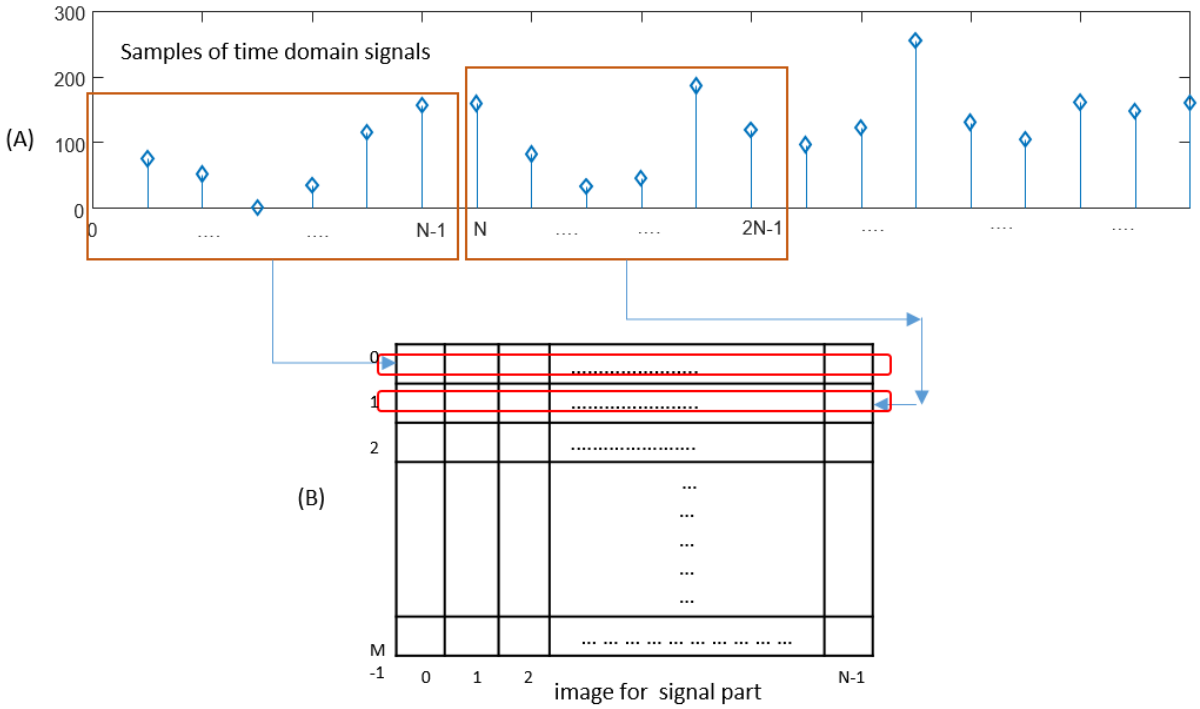

FIGURE 4. Conversion of signals to image: (A) A sample signal piece, (B) The image generated from signals.

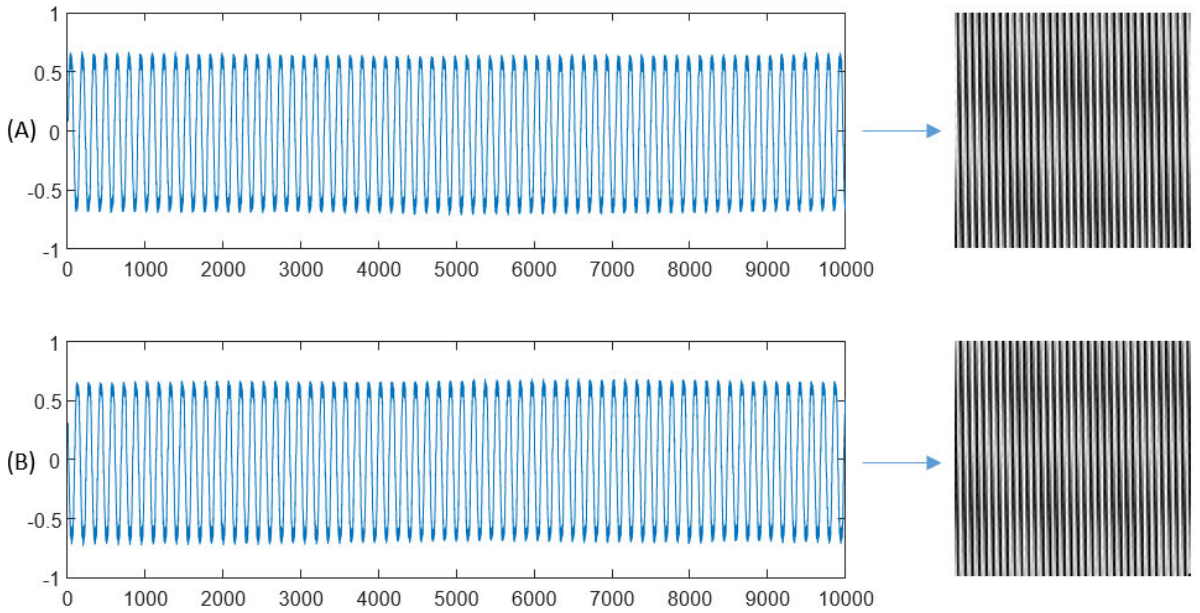

FIGURE 5. Conversion of a signal to a gray image of 100 × 100: (A) Faulty, (B) healthy single-phase current signals.

value. It has been demonstrated that axial flux coreless PMSGs can be used in the detection of current and voltage signals.

A. FAULT DETECTION USING CURRENT SIGNALS

Fig.7 includes the textural images formed as a result of the process of transforming the faulty and healthy axial flux coreless PMSG into images of the faulty and healthy signals belonging to 3 phases of no-load current signals taken at 600 rpm with 3% fault rate.

Fig.7 shows that the images of healthy and faulty signals are separated from each other. The texture is a property of the surface of an image. It can be expressed as a regular repetition of a texture or pattern on the image surface.

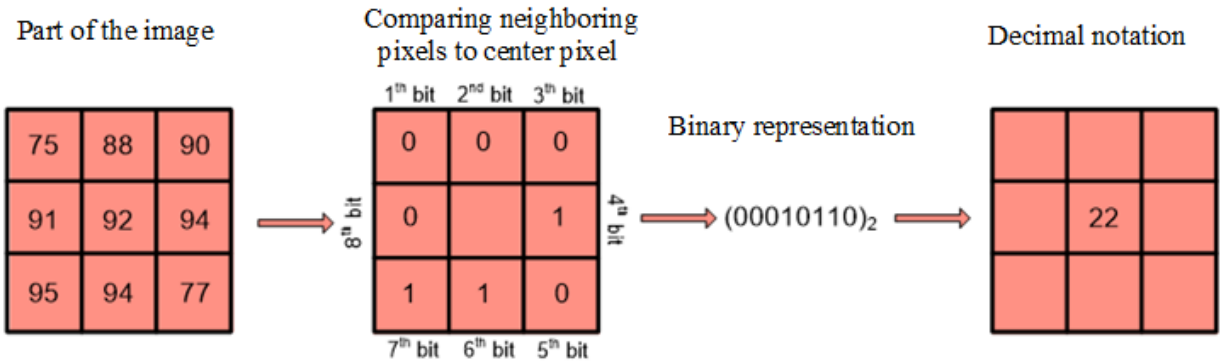

FIGURE 6. A sample computation of the LBP operator [39].

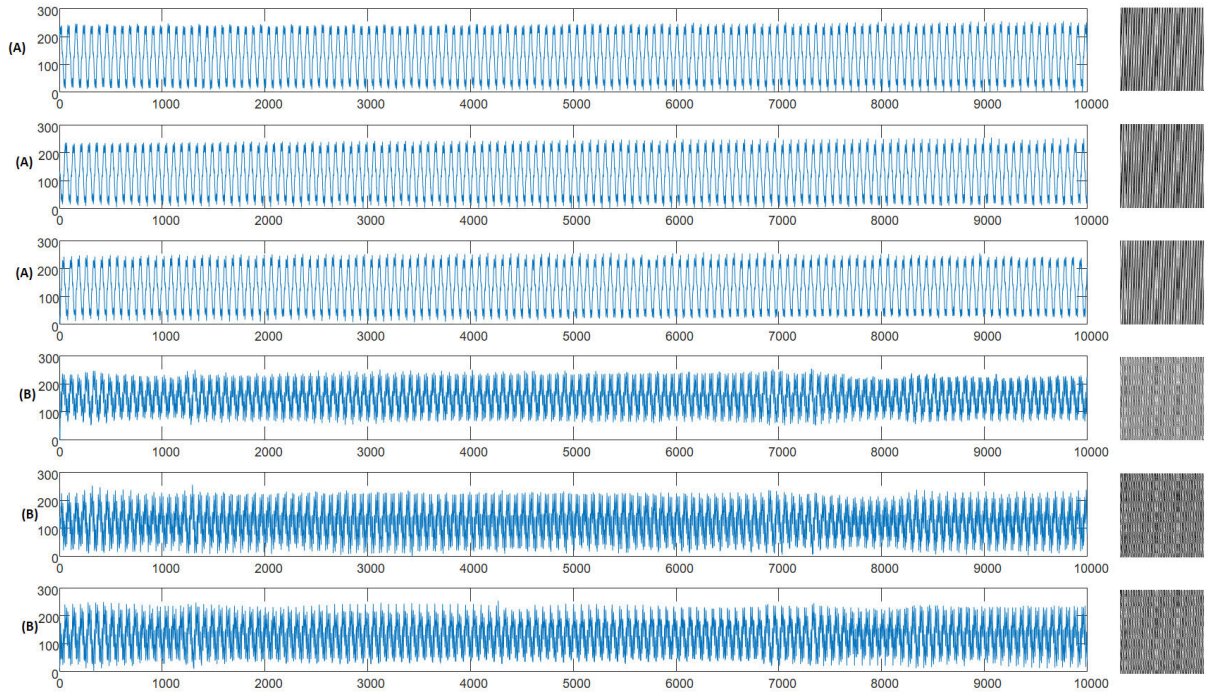

FIGURE 7. Conversion of single phase current signals to gray-level images. The signals were taken under 0 load at a speed of 600 rpm. (A) Faulty signals of 3% fault rate, (B) Healthy signals of 3% fault rate.

After the images of the signals were created by hand, the features were obtained from these images through the LBP. By using these feature vectors, the classification with Knn, in other words, the separation of healthy and faulty signals from each other, was performed. Procedures of the proposed fault diagnosis system were carried out for signals obtained under different fault, speed, and load conditions. The success rates obtained for each phase of the 3-phase current signals are given in Table 2-4.

In Table-2, success rates for 3% and 6% fault rates at different speeds and loads for the 1st phase current are given. It was understood that as the speed and loading rate increase at 3% fault rates, the fault detection rate also increases. The success rate achieved here was found to be approximately 98.34%. At the 6% fault rate, it was determined that the faults were separated depending on the speed and loading, and the success rate was 98.83%. When the loading rate was 35%, the faulty and healthy signals were observed to be completely separated from each other.

Success rates for the 2nd phase current are given in Table-3. It was found that as the speed and loading rate increases in 3% fault rates, the fault detection rate also increases. There is only a difference in the success rate at 0% loading. The success rate obtained was found to be approximately 99.33%. At the 6% fault rate, it was revealed that the faults did not differ significantly depending on the speed and loading, and the success rate was 100% in all of them.

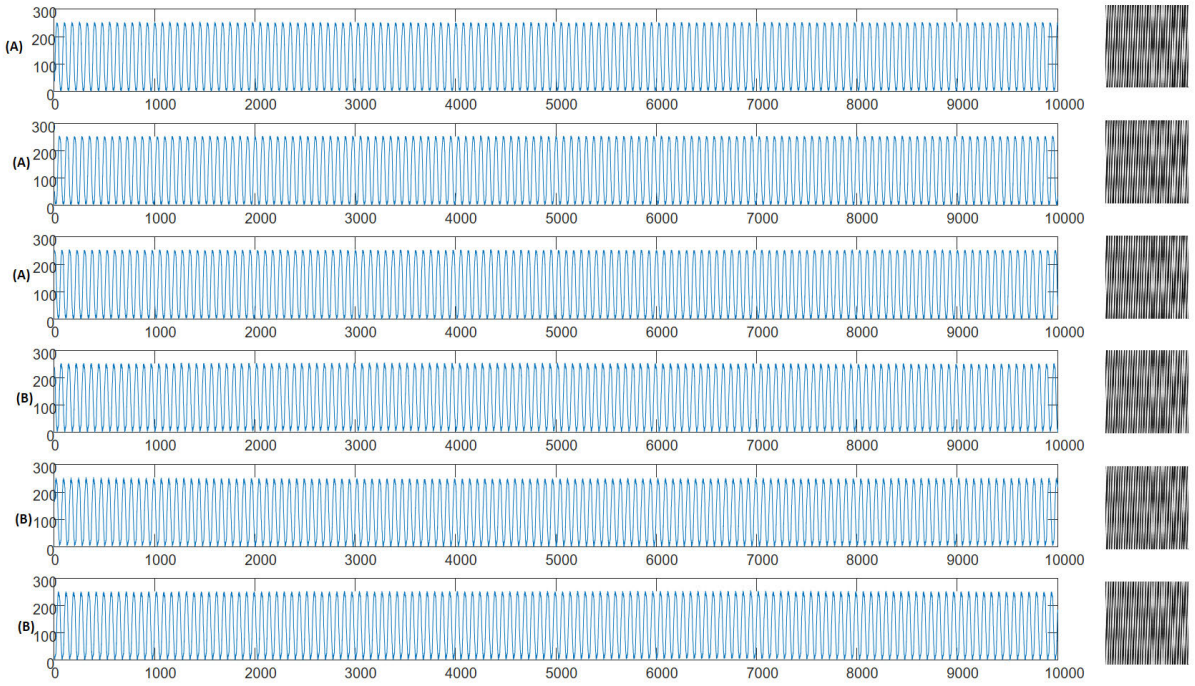

FIGURE 8. Conversion of voltage signals to gray-level images. The signals were taken under 0 load at a speed of 600 rpm. (A) Faulty signals of 3% fault rate, (B) Healthy signals of 3% fault rate.

TABLE 2. Current Signal Success Rates for Phase 1.

	%3 Fault rate				
Load	**300**	**400**	**500**	**600**	**Av. Acc.**
%0 Load	86.7	90	100	100	**95.75**
%35 Load	100	100	100	100	**100**
%70 Load	100	96.67	100	100	**99.17**
%100 Load	100	93.33	100	100	**98.33**
%115 Load	100	100	100	100	**100**
Av. Acc.	**97.34**	**96**	**100**	**100**	**98.34**
	%6 Fault rate				
Load	**300**	**400**	**500**	**600**	**Av. Acc.**
%0 Load	93.33	90	100	93.33	**94,17**
%35 Load	100	100	100	100	**100**
%70 Load	100	100	100	100	**100**
%100 Load	100	100	100	100	**100**
%115 Load	100	100	100	100	**100**
Av. Acc.	**98.66**	**98**	**100**	**98.66**	**98,83**

TABLE 3. Current Signal Success Rates for Phase 2.

	%3 Fault rate				
Load	**300**	**400**	**500**	**600**	**Av. Acc.**
%0 Load	93.33	93.33	100	100	**96,66**
%35 Load	100	100	100	100	**100**
%70 Load	100	100	100	100	**100**
%100 Load	100	100	100	100	**100**
%115 Load	100	100	100	100	**100**
Av. Acc.	**98.66**	**98.66**	**100**	**100**	**99,33**
	%6 Fault rate				
Load	**300**	**400**	**500**	**600**	**Av. Acc.**
%0 Load	100	100	100	100	**100**
%35 Load	100	100	100	100	**100**
%70 Load	100	100	100	100	**100**
%100 Load	100	100	100	100	**100**
%115 Load	100	100	100	100	**100**
Av. Acc.	**100**	**100**	**100**	**100**	**100**

Success rates for the 3rd phase current are given in Table-4. It was found that as the speed and loading rate increases at 3% fault rates, the fault detection rate also increases. There is only 0% loading at 3% fault and 76.67% success at 300 rpm. The average success rate obtained was found to be about 97.16%. High success rates were achieved at a fault rate of 6%. The success rate achieved here was determined as 98.33%. Looking at Table-2-4, it cannot be said that the percentage of success is directly related to speed, that is, no information can be given about the success of fault detection with the increase or decrease in speed. However, it is noteworthy that

TABLE 4. Current Signal Success Rates for Phase 3.

	%3 Fault rate				
Load	**300**	**400**	**500**	**600**	**Av. Acc.**
%0 Load	76.67	80	100	100	**89.16**
%35 Load	100	100	100	96.67	**99,16**
%70 Load	100	100	100	100	**100**
%100 Load	100	90	100	100	**97.5**
%115 Load	100	100	100	100	**100**
Av. Acc.	**95.33**	**94**	**100**	**99.33**	**97.16**
	%6 Fault rate				
Load	**300**	**400**	**500**	**600**	**Av. Acc.**
%0 Load	90	90	100	96.67	**94.17**
%35 Load	100	100	100	96.67	**99.16**
%70 Load	100	100	100	100	**100**
%100 Load	100	100	100	93.33	**98.33**
%115 Load	100	100	100	100	**100**
Av. Acc.	**98**	**98**	**100**	**97.33**	**98.33**

TABLE 5. Voltage Signals Success Rates for Phase 1.

	%3 Fault rate				
Load	**300**	**400**	**500**	**600**	**Av. Acc.**
%0 Load	83.33	100	100	100	**95.83**
%35 Load	100	100	100	100	**100**
%70 Load	100	100	100	100	**100**
%100 Load	100	100	100	100	**100**
%115 Load	100	100	100	100	**100**
Av. Acc.	**96.66**	**100**	**100**	**100**	**99.16**
	%6 Fault rate				
Load	**300**	**400**	**500**	**600**	**Av. Acc.**
%0 Load	100	100	100	100	**100**
%35 Load	100	100	100	100	**100**
%70 Load	100	100	100	100	**100**
%100 Load	100	100	100	100	**100**
%115 Load	100	100	100	100	**100**
Av. Acc.	**100**	**100**	**100**	**100**	**100**

the success rate in fault detection depending on the load is more proportional to the load. It is seen that fault detection shows a higher success graph, especially when the load rate rises above 0.

B. FAULT DETECTION USING VOLTAGE SIGNALS

Fig. 7 shows the textural images formed as a result of the process of transforming the faulty and healthy axial flux PMSG 3-phase unloaded three-phase voltage signals at 600 rpm with

TABLE 6. Voltage Signals Success Rates for Phase 2.

	%3 Fault rate				
Load	**300**	**400**	**500**	**600**	**Av. Acc.**
%0 Load	70	100	100	100	**92.5**
%35 Load	100	100	100	100	**100**
%70 Load	100	100	100	100	**100**
%100 Load	100	100	100	100	**100**
%115 Load	100	100	100	100	**100**
Av. Acc.	**94**	**100**	**100**	**100**	**98.5**
	%6 Fault rate				
Load	**300**	**400**	**500**	**600**	**Av. Acc.**
%0 Load	100	100	100	100	**100**
%35 Load	100	100	100	100	**100**
%70 Load	100	100	100	100	**100**
%100 Load	100	100	100	100	**100**
%115 Load	100	100	100	100	**100**
Av. Acc.	**100**	**100**	**100**	**100**	**100**

TABLE 7. Voltage Signals Success Rates for Phase 3.

	%3 Fault rate				
Load	**300**	**400**	**500**	**600**	**Av. Acc.**
%0 Load	80	100	100	100	**95**
%35 Load	100	100	100	100	**100**
%70 Load	100	100	100	100	**100**
%100 Load	96.67	100	100	100	**99.16**
%115 Load	100	100	100	100	**100**
Av. Acc.	**95.33**	**100**	**100**	**100**	**98.83**
	%6 Fault rate				
Load	**300**	**400**	**500**	**600**	**Av. Acc.**
%0 Load	100	100	100	100	**100**
%35 Load	100	100	100	100	**100**
%70 Load	100	100	100	100	**100**
%100 Load	100	100	100	100	**100**
%115 Load	100	100	100	100	**100**
Av. Acc.	**100**	**100**	**100**	**100**	**100**

3% fault rate to images of the faulty and normal signals of 3 phases.

Fig.8. shows that the textures contained in the images of voltage signals for healthy and faulty axial flux coreless PMSG are separated from each other. The operations of the proposed fault diagnosis system are carried out for signals obtained under different fault, speed, and load conditions. The

TABLE 8. Success Rates for Current Signals According to Different Radius Values for Phase 3.

R (Radius)	Load	300 rpm	400 rpm	500 rpm	600 rpm	Av. Acc.
R=1	%0 Load	76.67	80	100	100	**89.16**
	%35 Load	100	100	100	96.67	**99,16**
	%70 Load	100	100	100	100	**100**
	%100 Load	100	90	100	100	**97.5**
	%115 Load	100	100	100	100	**100**
R=2	%0 Load	86.67	96.67	100	100	**95.835**
	%35 Load	100	100	100	96.67	**99.1675**
	%70 Load	100	100	100	100	**100**
	%100 Load	100	90	100	100	**97.5**
	%115 Load	100	100	100	100	**100**
R=3	%0 Load	86.67	80	100	100	**91.6675**
	%35 Load	100	100	100	100	**100**
	%70 Load	100	100	100	100	**100**
	%100 Load	100	96.67	100	100	**99.1675**
	%115 Load	100	100	100	100	**100**

TABLE 9. Success Rates for Voltage Signals According to Different Radius Values for Phase 2.

R (Radius)	Load	300 rpm	400 rpm	500 rpm	600 rpm	Av. Acc.
R=1	%0 Load	70	100	100	100	**92.5**
	%35 Load	100	100	100	100	**100**
	%70 Load	100	100	100	100	**100**
	%100 Load	100	100	100	100	**100**
	%115 Load	100	100	100	100	**100**
R=2	%0 Load	86.67	100	100	100	**96.66**
	%35 Load	100	100	100	100	**100**
	%70 Load	100	100	100	100	**100**
	%100 Load	100	100	100	100	**100**
	%115 Load	100	100	100	100	**100**
R=3	%0 Load	70	100	100	100	**92.5**
	%35 Load	100	100	100	100	**100**
	%70 Load	100	100	100	100	**100**
	%100 Load	100	100	100	100	**100**
	%115 Load	100	100	100	100	**100**

success rates obtained for each phase of the 3-phase voltage signals are given in Table 5-7.

Table-5 shows success rates for 3% and 6% fault rates at different speeds and loads for the 1st phase voltage. At 3% fault rates, only the speed of 300 rpm and 0% loading had an effect on the success rate, and the average success rate was determined as 99.16%. At the 6% fault rate, it was revealed that the faults did not decompose depending on the speed and loading, and the success rate was 100% and decomposed completely in all of them.

Table-6 shows success rates for 3% and 6% fault rates at different speeds and loads for the 2nd phase voltage. At 3% fault rates, only the speed of 300 rpm and 0% loading had an effect on the success rate, and the average success rate was 98.5%. At the 6% fault rate, it was revealed that the faults did not decompose depending on the speed and loading, and the success rate was 100% and decomposed completely in all of them.

Table-7 shows success rates for 3% and 6% fault rates at different speeds and loads for the 3rd phase voltage. At 3% fault rates, only the speed of 300 rpm and 0% to 100% loading had an effect on the success rate, and the average success rate was found to be 98.83%. At the 6% fault rate, it was revealed that the faults did not decompose depending on the speed and loading, and the success rate was 100% and decomposed completely in all of them. In Table-5-7, it was revealed that the percentage of success is not related to speed. In the comparison of the faulty and healthy signals obtained in the axial flux PMSG, it was revealed that the generator does not depend on the speed and loading rate.

The LBP has two important parameters. The first parameter of the LBP is P, which specifies the number of neighbors. Large values of P in the creation of the LBP image both enlarge the feature histogram and increase the transaction cost. Small values of P can cause significant information loss. The second parameter of the LBP is the scale (R) parameter. R indicates the distance of neighboring pixels from the center pixel. By using different R values, it is possible to analyse texture of different scales. Features according to different R values were obtained from the images created from the current and voltage signals. The success rates observed for the current signals containing 6% fault in Phase 3 and different values of R are given

TABLE 10. The Reported Studies on the Stator Fault.

Referans	Model	Dataset	Fault Type	Accuracy
[45]	Hilbert Huang transform	Simulation	Permanent magnet Machine	-
[46]	Pattern identification	Simulation	Permanent magnet Machine	92.1%
[47]	Wavelet transform	Simulation	Permanent magnet Machine	93.2%
[48]	Artificial neural networks	Original	Permanent magnet Machine	-
[49]	SOM neural networks	Original	Permanent magnet Machine	93.25%
[50]	Fast Fourier transform	Original	Induction Machine	97.5%
[51]	Random forest	Original	Permanent magnet Machine	98.1%
[52]	Signal2Image+LBPs	Original	Servo motor	95.93-100%
	Image texture analysis			
[31]	LBP based texture analysis	Original	Induction motors	84.375-100%
[36]	Image texture analysis	Original	Wind turbine	98%
[53]	Unscented Kalman Filter	Simulation	Permanent magnet Machine	100%
This Study	Image texture analysis	Simulation	Axial Flux PMSG	97.16-100%

in Table 8. The results observed for different values of R and voltage signals with 6% failure in Phase 2 are given in Table 9.

Tables show that high success rates were observed for all values of R for both current and voltage signals. The value of R should be decided after trials.

C. COMPARISON OF THE OBTAINED RESULTS WITH LITERATURE

Table 10 gives information about studies on the detection of machine faults. As can be seen from the table, fault detection success rates ranged from 92.1% to 100%. In this study, an effective method was proposed for the demagnetization detection using solely the current and voltage data. This study presents a high accuracy rate of fault detection with the texture-based analysis method. Tests were conducted for the signals of current and voltage obtained from the axial flux coreless PMSM when operating under different speeds and loads. According to the obtained results, high success rates were obtained in the classification of demagnetization faults by the proposed feature extraction method with the Knn classifier.

V. DISCUSSION

In this study, voltage and current signals were taken from faulty and healthy axial flux coreless PMSGs at different speeds and loading rates. A texture analysis-based approach, which is an effective feature extraction approach, has been proposed for the decomposition of these signals. Axial flux coreless PMSG current and voltage signals were transformed into two-dimensional grayscale images. Time-domain signals can be converted into images in desired MxN dimensions. Then, texture features are obtained from these images with LBP. Fault detection was carried out with different machine learning methods using these features.

A literature review shows that there are many studies that are conducted using ready-made data sets for different feature extraction schemes and fault classification techniques. Demagnetization of fault depending on the speed and the load AFPMG models were created. An effective feature extraction method based on texture analysis has been proposed for current and voltage signals. Current and voltage signals were first converted to grayscale images. It is understood from the images that the signals of different faults form different textures. Then, texture features are obtained from these images

with the LBP. These features are classified using different machine learning methods by current and voltage signals.

In the loading and speed trials carried out in axial flux coreless PMSG, it has been revealed that the detection of faulty and healthy signals does not depend on the load. It has been seen that the success rate of the machine at 300 rpm and 0% loads slightly decreased. When comparing the success of current and voltage signals in fault decomposition, it was seen that the success in voltage signals is slightly higher than current. However, when all the results are evaluated together, it has been shown that neither the loading rate nor the speed of the machine is effective in decomposing the faulty and solid signals in the axial flux coreless PMSG.

It will be used in the classification of different fault types with the approach suggested in our next studies. In addition, it will be tested in the classification of signals with large values of fault rates.

REFERENCES

[1] M. R. Minaz and M. Çelebi, "Design and analysis of a new axial flux coreless PMSG with three rotors and double stators," *Results Phys.*, vol. 7, pp. 183–188, 2017, doi: 10.1016/j.rinp.2016.10.026.

[2] K. Sitapati and R. Krishnan, "Performance comparisons of radial and axial field, permanent-magnet, brushless machines," *IEEE Trans. Ind. Appl.*, vol. 37, no. 5, pp. 1219–1226, 2001, doi: 10.1109/28.952495.

[3] S. Kahourzade, A. Mahmoudi, H. W. Ping, and M. N. Uddin, "A comprehensive review of axial-flux permanent-magnet machines," *Can. J. Elect. Comput. Eng.*, vol. 37, no. 1, pp. 19–33, 2014.

[4] Y. Jeong, S.-K. Sul, S. E. Schulz, and N. R. Patel, "Fault detection and fault-tolerant control of interior permanent-magnet motor drive system for electric vehicle," *IEEE Trans. Ind. Appl.*, vol. 41, no. 1, pp. 46–51, Jan. 2005, doi: 10.1109/TIA.2004.840947.

[5] B. Boazzo, G. Pellegrino, and A. Vagati, "Multipolar SPM machines for direct-drive application: A general design approach," *IEEE Trans. Ind. Appl.*, vol. 50, no. 1, pp. 327–337, Jan. 2014, doi: 10.1109/TIA.2013.2271291.

[6] J. Faiz and E. Mazaheri-Tehrani, "Demagnetization modeling and fault diagnosing techniques in permanent magnet machines under stationary and nonstationary conditions: An overview," *IEEE Trans. Ind. Appl.*, vol. 53, no. 3, pp. 2772–2785, May 2017, doi: 10.1109/TIA.2016.2608950.

[7] X. Li and W. Shuhong, "Demagnetization analysis of the interior permanent magnet synchronous motor under different short circuit faults," *J. China Coal Soc.*, vol. 42, no. S2, pp. 626–632, 2017.

[8] J. K. Si, L. F. Zheng, and H. C. Feng, "Analysis of 3-D temperature field for surface-mounted and interior permanent magnet synchronous motor," *Electr. Mach. Control*, vol. 21, no. 3, pp. 25–31, 2017.

[9] M. Eker and M. Akar, "A novel approach for demagnetization fault diagnosis in permanent magnet synchronous motors sabit Mıknatıslı Senkron Motorlarda Demagnetizasyon Arızasının Tespiti için Yeni bir Yaklaşım," *J. New Results Eng. Nat. Sci.*, vol. 1, no. 1, pp. 1–13, 2013.

[10] S. Yu and T. Ren, "Electromagnetic and mechanical characterizations of noise and vibration in permanent magnet synchronous machines," *IEEE Trans. Magn.*, vol. 42, no. 4, pp. 1335–1338, Apr. 2006, doi: 10.1109/TMAG.2006.871637.

[11] J. Hur, "Characteristic analysis of interior permanent-magnet synchronous motor in electrohydraulic power steering systems," *IEEE Trans. Ind. Electron.*, vol. 55, no. 6, pp. 2316–2323, Jun. 2008, doi: 10.1109/TIE.2008.918402.

[12] J. Wang, W. Wang, K. Atallah, and D. Howe, "Demagnetization assessment for three-phase tubular brushless permanent-magnet machines," *IEEE Trans. Magn.*, vol. 44, no. 9, pp. 2195–2203, Sep. 2008, doi: 10.1109/TMAG.2008.2001074.

[13] K. M. Siddiqui and S. Chatterji, "Early, demagnetization assessment of PMSM," *J. Circuits Syst.*, vol. 6, no. 4, pp. 16–25, 2018.

[14] A. Sarikhani and O. Mohammed, "Real-time demagnetization assessment of PM synchronous machine," in *Proc. 20th Int. Conf. Electr. Mach.*, vol. 2, no. 1, Sep. 2012, pp. 2418–2424, doi: 10.1109/ICElMach.2012.6350222.

[15] S. Ruoho, J. Kolehmainen, J. Ikaheimo, and A. Arkkio, "Interdependence of demagnetization, loading, and temperature rise in a permanent-magnet synchronous motor," *IEEE Trans. Magn.*, vol. 46, no. 3, pp. 949–953, Mar. 2010, doi: 10.1109/TMAG.2009.2033592.

[16] W. Qiao and D. Lu, "A survey on wind turbine condition monitoring and fault diagnosis—Part I: Components and subsystems," *IEEE Trans. Ind. Electron.*, vol. 62, no. 10, pp. 6536–6545, Oct. 2015, doi: 10.1109/TIE.2015.2422112.

[17] S. Simani, S. Farsoni, and P. Castaldi, "Fault diagnosis of a wind turbine benchmark via identified fuzzy models," *IEEE Trans. Ind. Electron.*, vol. 62, no. 6, pp. 3775–3782, Jun. 2015, doi: 10.1109/TIE.2014.2364548.

[18] M. Eker, M. Akar, C. Emeksiz, and Z. Doğan, "A novel method for partial demagnetization fault detection in PMSMs SMSM ' de Kısmi Demagnetizasyon Arızasının Tespiti için Yeni Bir Yaklaşım," Tech. Rep., 2017.

[19] G. Feng, C. Lai, and N. C. Kar, "Particle-filter-based magnet flux linkage estimation for PMSM magnet condition monitoring using harmonics in machine speed," *IEEE Trans. Ind. Informat.*, vol. 13, no. 3, pp. 1280–1290, Jun. 2017, doi: 10.1109/TII.2016.2616331.

[20] M. Zhu, W. Hu, and N. C. Kar, "Multi-sensor fusion-based permanent magnet demagnetization detection in permanent magnet synchronous machines," *IEEE Trans. Magn.*, vol. 54, no. 11, pp. 1–6, Nov. 2018, doi: 10.1109/TMAG.2018.2836182.

[21] J. De Bisschop, A. Abdallh, P. Sergeant, and L. Dupre, "Identification of demagnetization faults in axial flux permanent magnet synchronous machines using an inverse problem coupled with an analytical model," *IEEE Trans. Magn.*, vol. 50, no. 11, pp. 8–11, Dec. 2014, doi: 10.1109/TMAG.2014.2316851.

[22] E. Ajily, M. Ardebili, and K. Abbaszadeh, "Magnet defect and rotor eccentricity modeling in axial-flux permanent-magnet machines via 3-D field reconstruction method," *IEEE Trans. Energy Convers.*, vol. 31, no. 2, pp. 486–495, Jun. 2016, doi: 10.1109/TEC.2015.2506819.

[23] H. Saavedra, J.-R. Riba, and L. Romeral, "Magnet shape influence on the performance of AFPMM with demagnetization," in *Proc. 39th Annu. Conf. IEEE Ind. Electron. Soc. (IECON)*, Nov. 2013, pp. 973–977, doi: 10.1109/IECON.2013.6699265.

[24] M. S. Khadim and S. Chatterji, "Demagnetization diagnosis in multi-phase PMSM machine by advanced MCSA technique," *i-Manager's J. Electr. Eng.*, vol. 12, no. 4, p. 37, 2019, doi: 10.26634/jee.12.4.15758.

[25] J. A. Rosero, J. Cusido, A. Garcia, J. A. Ortega, and L. Romeral, "Broken bearings and eccentricity fault detection for a permanent magnet synchronous motor," in *Proc. 32nd Annu. Conf. IEEE Ind. Electron. (IECON)*, Nov. 2006, pp. 964–969, doi: 10.1109/IECON.2006.347599.

[26] J. Z. Liu, X. H. Yu, S. H. Wang, and M. C. Sun, "Study on permanent magnet demagnetization characteristics in permanent magnet synchronous machines," in*Proc. 32nd Annu. Conf. IEEE Ind. Electron. Soc.*, Paris, France, vols. 211–212, 2006, pp. 879–884, doi: 10.4028/www.scientific.net/AMR.211-212.127.

[27] A. G. Espinosa, J. A. Rosero, J. Cusido, L. Romeral, and J. A. Ortega, "Fault detection by means of Hilbert–Huang transform of the stator current in a PMSM with demagnetization," *IEEE Trans. Energy Convers.*, vol. 25, no. 2, pp. 312–318, Jun. 2010, doi: 10.1109/TEC.2009.2037922.

[28] M. Zhu, B. Yang, W. Hu, G. Feng, and N. C. Kar, "Vold–Kalman filtering order tracking based rotor demagnetization detection in PMSM," *IEEE Trans. Ind. Appl.*, vol. 55, no. 6, pp. 5768–5778, Nov. 2019, doi: 10.1109/tia.2019.2932692.

[29] M. Zhu, W. Hu, and N. C. Kar, "Torque-ripple-based interior permanent-magnet synchronous machine rotor demagnetization fault detection and current regulation," *IEEE Trans. Ind. Appl.*, vol. 53, no. 3, pp. 2795–2804, May 2017, doi: 10.1109/TIA.2016.2634518.

[30] K. Kaplan, Y. Kaya, M. Kuncan, M. R. Minaz, and H. M. Ertunç, "An improved feature extraction method using texture analysis with LBP for bearing fault diagnosis," *Appl. Soft Comput.*, vol. 87, Feb. 2020, Art. no. 106019, doi: 10.1016/j.asoc.2019.106019.

[31] M. R. Shahriar, T. Ahsan, and U. Chong, "Fault diagnosis of induction motors utilizing local binary pattern-based texture analysis," *EURASIP J. Image Video Process.*, vol. 2013, no. 1, pp. 1–11, Dec. 2013, doi: 10.1186/1687-5281-2013-29.

[32] Y. Kaya, M. Kuncan, K. Kaplan, M. R. Minaz, and H. M. Ertunç, "Classification of bearing vibration speeds under 1D-LBP based on eight local directional filters," *Soft Comput.*, vol. 24, no. 16, pp. 12175–12186, Aug. 2020, doi: 10.1007/s00500-019-04656-2.

[33] Y. Kaya, M. Kuncan, K. Kaplan, M. R. Minaz, and H. M. Ertunç, "A new feature extraction approach based on one dimensional gray level co-occurrence matrices for bearing fault classification," *J. Exp. Theor. Artif. Intell.*, pp. 1–18, 2020.

[34] M. Kuncan, K. Kaplan, M. R. Minaz, Y. Kaya, and H. M. Ertunç, "A novel feature extraction method for bearing fault classification with one dimensional ternary patterns," *ISA Trans.*, vol. 100, pp. 346–357, May 2020, doi: 10.1016/j.isatra.2019.11.006.

[35] M. Kuncan, "An intelligent approach for bearing fault diagnosis: Combination of 1D-LBP and GRA," *IEEE Access*, vol. 8, pp. 137517–137529, 2020, doi: 10.1109/ACCESS.2020.3011980.

[36] M. Ruiz, L. E. Mujica, S. Alférez, L. Acho, C. Tutivén, Y. Vidal, J. Rodellar, and F. Pozo, "Wind turbine fault detection and classification by means of image texture analysis," *Mech. Syst. Signal Process.*, vol. 107, pp. 149–167, Jul. 2018, doi: 10.1016/j.ymssp.2017.12.035.

[37] T. Ojala, M. Pietikainen, and T. Maenpaa, "Multiresolution gray-scale and rotation invariant texture classification with local binary patterns," *IEEE Trans. Pattern Anal. Mach. Intell.*, vol. 24, no. 7, pp. 971–987, Jul. 2002, doi: 10.1109/TPAMI.2002.1017623.

[38] G. Zhao and M. Pietik, "Patterns with an application to facial expressions," *Most*, vol. 29, no. 6, pp. 1–14, 2007. [Online]. Available: http://www.computer.org/portal/web/csdl/doi/10.1109/TPAMI.2007.1110

[39] Y. Kaya, Ö. F. Ertuğrul, and R. Tekin, "Two novel local binary pattern descriptors for texture analysis," *Appl. Soft Comput.*, vol. 34, pp. 728–735, Sep. 2015, doi: 10.1016/j.asoc.2015.06.009.

[40] L. Nanni, S. Brahnam, and A. Lumini, "A simple method for improving local binary patterns by considering non-uniform patterns," *Pattern Recognit.*, vol. 45, no. 10, pp. 3844–3852, Oct. 2012, doi: 10.1016/j.patcog.2012.04.007.

[41] F. Kuncan, Y. Kaya, and M. Kuncan, "A novel approach for activity recognition with down-sampling 1D local binary pattern features," *Adv. Electr. Comput. Eng.*, vol. 19, no. 1, pp. 35–44, 2019, doi: 10.4316/AECE.2019.01005.

[42] F. Kuncan, Y. Kaya, and M. Kuncan, "New approaches based on local binary patterns for gender identification from sensor signals," *J. Fac. Eng. Archit. Gazi Univ.*, vol. 34:4, pp. 2173–2185, Jun. 2019, doi: 10.17341/gazimmfd.426259.

[43] S. Fekri-Ershad, "Bark texture classification using improved local ternary patterns and multilayer neural network," *Expert Syst. Appl.*, vol. 158, Nov. 2020, Art. no. 113509.

[44] S. Fekri-Ershad and F. Tajeripour, "Multi-resolution and noise-resistant surface defect detection approach using new version of local binary patterns," *Appl. Artif. Intell.*, vol. 31, nos. 5–6, pp. 395–410, Jul. 2017.

[45] J. Rosero, L. Romeral, J. A. Ortega, and J. C. Urresty, "Demagnetization fault detection by means of Hilbert Huang transform of the stator current decomposition in PMSM," in *Proc. IEEE Int. Symp. Ind. Electron.*, Jun. 2008, pp. 172–177, doi: 10.1109/ISIE.2008.4677217.

[46] B. M. Ebrahimi, J. Faiz, and B. N. Araabi, "Pattern identification for eccentricity fault diagnosis in permanent magnet synchronous motors using stator current monitoring," *IET Electr. Power Appl.*, vol. 4, no. 6, p. 418, 2010, doi: 10.1049/iet-epa.2009.0149.

[47] B. M. Ebrahimi, M. Javan Roshtkhari, J. Faiz, and S. V. Khatami, "Advanced eccentricity fault recognition in permanent magnet synchronous motors using stator current signature analysis," *IEEE Trans. Ind. Electron.*, vol. 61, no. 4, pp. 2041–2052, Apr. 2014, doi: 10.1109/TIE.2013.2263777.

[48] S. S. Moosavi, A. Djerdir, Y. Ait-Amirat, and D. A. Khaburi, "ANN based fault diagnosis of permanent magnet synchronous motor under stator winding shorted turn," *Electr. Power Syst. Res.*, vol. 125, pp. 67–82, Aug. 2015, doi: 10.1016/j.epsr.2015.03.024.

[49] C. Chuang, Z. Wei, W. Zhifu, and L. Zhi, "The diagnosis method of stator winding faults in PMSMs based on SOM neural networks," *Energy Procedia*, vol. 105, pp. 2295–2301, May 2017, doi: 10.1016/j.egypro.2017.03.663.

[50] J. R. Rivera-Guillen, J. J. De Santiago-Perez, J. P. Amezquita-Sanchez, M. Valtierra-Rodriguez, and R. J. Romero-Troncoso, "Enhanced FFT-based method for incipient broken rotor bar detection in induction motors during the startup transient," *Measurement*, vol. 124, pp. 277–285, Aug. 2018, doi: 10.1016/j.measurement.2018.04.039.

[51] J. C. Quiroz, N. Mariun, M. R. Mehrjou, M. Izadi, N. Misron, and M. A. Mohd Radzi, "Fault detection of broken rotor bar in LS-PMSM using random forests," *Measurement*, vol. 116, pp. 273–280, Feb. 2018, doi: 10.1016/j.measurement.2017.11.004.

[52] K. Kaplan, M. Kuncan, and H. M. Ertunc, "Prediction of bearing fault size by using model of adaptive neuro-fuzzy inference system," in *Proc. 23nd Signal Process. Commun. Appl. Conf. (SIU)*, May 2015, pp. 1925–1928, doi: 10.1109/SIU.2015.7130237.

[53] N. Zhou, H. He, Z. Liu, and Z. Zhang, "UKF-based sensor fault diagnosis of PMSM drives in electric vehicles," *Energy Procedia*, vol. 142, pp. 2276–2283, Dec. 2017, doi: 10.1016/j.egypro.2017.12.630.

MEHMET RECEP MİNAZ received the bachelor's degree from the Department of Electrical and Electronics Engineering, Dicle University, the master's degree from the Department of Electrical and Electronics Engineering, Bilecik Şeyh Edebali University, and the Ph.D. degree from the Department of Electrical and Electronics Engineering, Atatürk University, Turkey. Since 2017, he has been a Faculty Member with the Department of Electrical and Electronics Engineering, Siirt University. His current research interests include electric machines and energy transformation, electric energy and power systems, and data mining.

EYYÜP AKCAN received the bachelor's degree from the Department of Electrical and Electronics Engineering, Siirt University, Turkey, and the master's degree in electrical and electronics engineering from Siirt University. His current research interests include electric machines and energy transformation, electric energy and power systems, and data mining.